Near-bed turbulence and bottom friction during SandyDuck97

C. Smyth and Alex E. Hay

Department of Oceanography, Dalhousie University, Halifax, Nova Scotia, Canada

Received 30 April 2001; revised 5 January 2003; accepted 30 January 2003; published 20 June 2003.

[1] Remote acoustic measurements of turbulence intensity profiles are investigated as a function of wave energy and bedstate, from low energy vortex ripples to high energy flat bed. Outside the wave boundary layer, velocity power spectral densities increase with increasing wave energy for all bedstates at frequencies across the wave and turbulence bands up to the Nyquist frequency of the measurements, 8 to 10 Hz. The power spectra of the horizontal and vertical velocity exhibit the $-5/3$ slope characteristic of inertial subrange turbulence. As the seafloor is approached, the slopes of the vertical velocity spectra in this subrange become progressively less steep, reaching values between -1.2 and -0.6 within the wave boundary layer where the spectral densities are independent of bedstate and incident wave energy. Consistent with laboratory turbulence spectra showing similarly reduced spectral roll-off for the transverse velocity component at microscale Reynolds numbers below 1000 [*Sreenivasan*, 1996], these field observations indicate that near-bed turbulence generated by irregular waves above a mobile bed is probably anisotropic. Ensemble-averaged vertical turbulence intensity profiles exhibit a peak within the wave boundary layer at heights of O(1 cm) above bottom for all bedstates. The peak is less pronounced for higher energy bedstates. Consistent with the observed spectral convergence within the boundary layer, these peak average turbulence intensities are relatively independent of bedstate, varying by no more than 50% despite a factor of 7 variation in average wave energy. This remarkable observation can be understood from the corresponding decrease in the physical roughness of the bed, associated with the different observed bedstates, as wave energy increases. Estimated wave friction factors are highest for low-energy rippled beds and smallest for flat bed conditions, and within the uncertainty of the measurements, are generally consistent with predictions from the model by *Tolman* [1994]. *INDEX TERMS:* 4568 Oceanography: Physical: Turbulence, diffusion, and mixing processes; 4546 Oceanography: Physical: Nearshore processes; 4558 Oceanography: Physical: Sediment transport

Citation: Smyth, C., and A. E. Hay, Near-bed turbulence and bottom friction during SandyDuck97, *J. Geophys. Res.*, *108*(C6), 3197, doi:10.1029/2001JC000952, 2003.

1. Introduction

[2] The processes by which turbulence entrains sediments from the seafloor and distributes them in the water column are poorly understood. In wave-dominated conditions (i.e., weak low-frequency currents), bed-induced turbulence is expected to be confined to a relatively thin bottom boundary layer, as observed in laboratory experiments [*Sleath*, 1987; *Jensen et al.*, 1989]. There are few direct measurements of turbulent velocities in the wave bottom boundary layer in natural environments [*Trowbridge and Agrawal*, 1995; *Foster et al.*, 2000; *Smyth et al.*, 2002], and even fewer instances in which turbulence measurements have been combined with quantitative measurements of the configuration of the mobile bed, that is, of the bedform geometry, or bedstate. Thus a quantitative description of the relationship between turbulence intensity and bedstate is lacking, especially for the irregular wave conditions and multiple-scale bedforms often encountered in the nearshore zone and on the continental shelf.

[3] The recent development of a Coherent Doppler Profiler (CDP) [*Zedel and Hay*, 1999] enables measurements of vertical velocity profiles with sub-centimeter vertical resolution at ensemble-averaged rates of 15–30 Hz, which is sufficient to resolve the larger scales of inertial subrange turbulence [*Zedel and Hay*, 1999; *Smyth et al.*, 2002]. Thus, from a sensor height of O(1 m) above bottom, the CDP provides remotely measured vertical profiles of turbulence intensity through the O(10 cm) thick wave bottom boundary to the seabed, with minimal disturbance of the near-bed flow.

[4] For this study, data were collected during the SandyDuck97 experiment for a variety of wave conditions over a 75-day period in the fall of 1997. Observations were separated by bedstate, which was quantified using acoustic rotary sonar data (A. E. Hay and T. D. Mudge, Bedstate and wave energy, skewness and asymmetry during SandyDuck97, manuscript in preparation, 2003). At any one

0148-0227/03/2001JC000952$09.00

location, there was generally a progression through the different bedstates with changing average wave energy: irregular ripples for the lowest energy waves, then cross ripples, then linear transition ripples, and finally flat bed for high-energy conditions. This progression is consistent with previous observations by *Hay and Wilson* [1994].

[5] The importance of bed roughness is recognized in presently available bed stress models. However, empirical estimates of the friction factor based on laboratory results vary by a factor of 10 from model to model [*Grant and Madsen*, 1982; *Swart*, 1974]. One of the objectives of this study is to estimate turbulence intensities and wave friction factors for different bedstates. In a similar experiment conducted in 1995 at Queensland Beach, N. S., turbulence intensities were found to be similar for the four bedstates, despite large differences in wave energy [*Smyth et al.*, 2002]. This result supports the view that ripple field adjustment is of key importance to turbulence levels above mobile beds. However, the Queensland data set was only 11 days long, included only one storm event, was dominated by long periods of low wave energy when the bed was inactive, and was obtained in a pocket beach environment at the head of a relatively sheltered coastal embayment [*Crawford and Hay*, 2001]. In order to more fully investigate the relationships among wave friction factor, bedstate, and wave energy for field data, and to test the generality of the previous findings from *Smyth et al.* [2002], turbulence intensities and wave friction factors are investigated here using the much more extensive SandyDuck97 data set from a high-energy, open coast environment on a linear barred beach.

[6] Previous investigations of turbulence in the wave bottom boundary layer have found spectral slopes close to $-5/3$ in the inertial subrange for the horizontal velocity power spectra [*Foster et al.*, 2000; *Conley and Inman*, 1992; *Sleath*, 1987]. In contrast, observations of vertical velocity power spectra indicate inertial subrange slopes less steep than $-5/3$ [*Smyth et al.*, 2002; *Hino et al.*, 1983]. One inference to be drawn from these results is that turbulence in the wave boundary layer may be anisotropic. One might further postulate that the degree of anisotropy is related to bedstate, assuming there to be a relationship between the bedform scale and the scales of the largest eddies. Thus a second objective of the present study is to investigate the dependence on bedstate and height above bottom of spectral roll-off in the small-scale, high-frequency tail of the vertical velocity power spectrum.

[7] The next section contains a brief summary of wave bottom boundary layer theory, bed stress, and the related wave friction factors. A description of the experiment and instruments is given in section 3. Velocity spectra are discussed in section 4, and turbulence intensity profiles are found in section 5. Predicted values of the wave friction factor are compared to the measurements in section 6.

2. Bed Stress Formulae

[8] The linearized equation of motion for flow in the x-z plane is given by

$$\rho \frac{\partial u}{\partial t} = -\frac{\partial p}{\partial x} + \frac{\partial \tau}{\partial z}, \tag{1}$$

where u is the horizontal velocity, ρ is the fluid density, p is the pressure and τ is the shear stress. As in the usual boundary layer approximation, the pressure gradient is assumed to be independent of z, giving in the boundary layer

$$\rho \frac{\partial}{\partial t}(u - u_\infty) = \frac{\partial \tau}{\partial z}, \tag{2}$$

where u_∞ is the free-stream velocity [see, e.g., *Jensen et al.*, 1989]. The maximum bed shear stress during a wave cycle is

$$\tau_0 = \rho u_*^2, \tag{3}$$

where u_* is the friction velocity. *Jonsson* [1966] defined a wave friction factor, f_w,

$$\tau_0 = \frac{1}{2}\rho f_w (A\omega)^2, \tag{4}$$

where A is the wave semi-excursion distance and ω is the wave angular frequency.

[9] There are several parameterizations for the friction factor. The first, from *Grant and Madsen* [1982], is obtained by solving equation (2) assuming a time-invariant eddy viscosity which increases linearly with height,

$$f_w = 0.08\left[\mathrm{Ker}^2 2\sqrt{\zeta_0} + \mathrm{Kei}^2 2\sqrt{\zeta_0}\right]^{-1} \tag{5}$$

where Ker and Kei are zeroth-order Kelvin functions [*Abramowitz and Stegun*, 1965, p. 379], and

$$\zeta_0 = \frac{1}{21.2\kappa\sqrt{f_w}}\frac{k_N}{2A}, \tag{6}$$

where κ is the von Kàrmàn constant and k_N is the wave-induced bed roughness which as described below, includes empirically derived parameterizations for the ripple roughness, k_r, at low wave-energy, and sheet-flow roughness, k_s, at high wave-energy. In the work by *Grant and Madsen* [1982], k_r is based on observations for monochromatic waves. *Tolman* [1994] uses the empirical relation from a later experiment [*Madsen et al.*, 1990], which indicated that irregular waves result in a hydrodynamically smoother bottom than monochromatic waves for identical ripple heights and height-to-length ratios,

$$k_r = 1.5A\left(\frac{\theta_d}{\theta_c}\right)^{-2.5}, \tag{7}$$

where θ_d is the grain roughness Shields parameter calculated using the grain diameter and θ_c is the critical Shields parameter for sediment motion. The grain roughness Shields parameter [*Nielsen*, 1992, p. 105] is defined by

$$\theta_d = \frac{1}{2}\frac{f_d A^2 \omega^2}{(s-1)g d_{50}}, \tag{8}$$

where f_d is the grain roughness friction factor based on equation (5) with k_N set to the median grain diameter, d_{50}, s is the sediment specific gravity, and g is the acceleration due

to gravity. The sheet-flow roughness, k_s, in the model by *Tolman* [1994] is the empirical relation from *Wilson* [1989],

$$k_s = 0.0655A\left(\frac{u_{1/3}^2}{(s-1)gA}\right)^{1.4}, \quad (9)$$

where $u_{1/3}$ is the significant wave orbital velocity, given by $2u_{rms}$ [*Thornton and Guza*, 1983].

[10] The second expression for the friction factor is from *Swart* [1974],

$$f_w = \exp\left[5.213\left(\frac{r}{A}\right)^{0.194} - 5.977\right], \quad (10)$$

where r is the bed roughness. The bed roughness may be taken as a grain roughness ($r = 2d_{50}$) or may be estimated as the equivalent bed roughness. The latter quantity can be estimated from the work of *Nielsen* [1992, p. 159],

$$r = \frac{8\eta^2}{\lambda} + 5\theta_{2.5}d_{50}, \quad (11)$$

where η is the bedform height, λ is the wavelength, d_{50} is the grain diameter, and $\theta_{2.5}$ is the grain roughness Shields parameter defined in a similar manner to θ_d. The addition of the grain roughness Shields parameter term takes into account the roughness contribution from moving sand grains. For flat bed conditions, $8\eta^2/\lambda$ is replaced by a grain roughness $2d_{50}$.

[11] Measurements of bed roughness, wave rms velocity, wave period and peak vertical turbulence intensity will be used to estimate the wave friction factor using equations 5 and 10 for comparison to the measured wave friction factors. The semi-excursion distance, A, is taken as $u_{1/3}/\omega$ for irregular waves, where ω is the energy-weighted mean angular frequency.

3. Experiment Description

3.1. Field Site

[12] Field data for this study were collected from August 26 to November 8, 1997, during the SandyDuck97 experiment. The site is a long linear beach located on the Outer Banks of North Carolina at the U.S. Army Corps of Engineers' Field Research Facility (FRF). Beach profiles were measured by the Coastal Research Amphibious Buggy (CRAB) during the experiment. Figure 1 shows mean beach profiles from the two CRAB lines parallel to the instrument line which was located at 995 m longshore distance in FRF coordinates; one 30 m to the north and the other 20 m to the south. The beach profile over yeardays 233 (August 21) to 301 (October 28) generally consisted of a two-bar system: a well-defined bar close to shore and a second smaller bar offshore. Instruments for which data are presented here were deployed between these two bars, at Stations B and C, nominally 1 m above the bottom in 3–4 m water depth (Figure 1).

[13] Sieve analysis of 11 short core tubes collected by divers within 20 m of frame B in the cross-shore direction and within 300 m in the longshore direction yielded the following grain diameters: d_{16} = 236 ± 32 μm, d_{50} = 170 ± 15 μm, d_{84} = 133 ± 9 μm where the subscripts denote "percent coarser than."

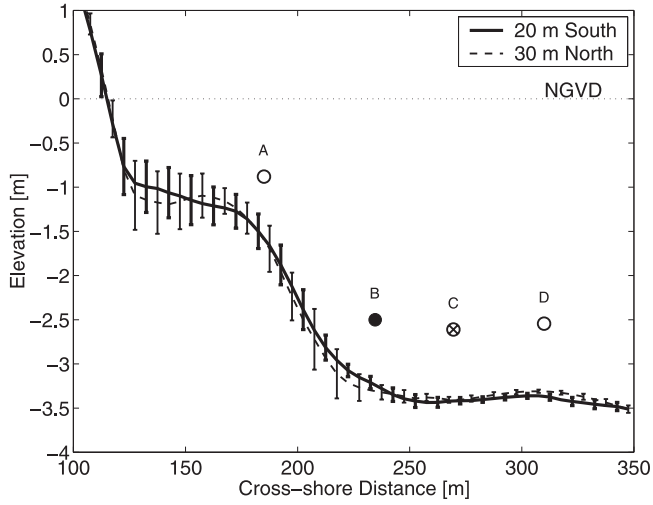

Figure 1. Mean cross-shore bottom profiles measured by the CRAB. Each mean profile is an average of 37 to 40 profiles, with error bars indicating the standard deviation about the mean. The locations of the four instrumented frames (A through D) are indicated by the circles. The CDP was on frame B.

[14] In the coordinate system used here, x and u are positive onshore, y and v are shore-parallel and positive southward, and z and w are positive upward from the seafloor.

3.2. Instrumentation

[15] The support frame consisted of an open framework of galvanized steel braces. This space-frame was clamped to four 7-m long, 6-cm diameter pipes which were jetted about 5 m into the bed. Instruments were positioned away from the support frame and bottom-piercing support pipes using a cantilevered mast (Figure 2). Instrumentation included a single-beam Coherent Doppler Profiler (CDP) system, two rotary pencil beam sonars and an Acoustic Doppler Velocimeter (ADV) located on the same instrument frame, and a rotary fan beam and pencil-beam sonar located on a nearby frame (Station C). The instruments are briefly described below, but interested readers are referred to more thorough descriptions elsewhere: CDP [*Zedel et al.*, 1996; *Zedel and Hay*, 1998, 1999] and rotary sonars [*Hay and Wilson*, 1994; *Wilson and Hay*, 1995; *Ngusaru*, 2000].

[16] The 1.7-MHz Coherent Doppler Profiler measures O(1 m) vertical profiles of particle velocity and concentration with 0.7-cm vertical resolution. Data runs approximately 20 min long were collected hourly during storm conditions and every other hour otherwise. The sampling rate of the ensemble-averaged profile (average of 25 profiles) was 16 Hz to 20 Hz, and was optimized relative to distance above bottom which ranged from 0.75 to 1 m. Particles in the acoustic beam backscatter the sound which is then received by the transducer. The velocity of the particles is determined from the change in phase of the backscattered sound between successive pulses. A characteristic speed ambiguity results when the phase change exceeds ±180 degrees. Velocities that exceed the ambiguity velocity are

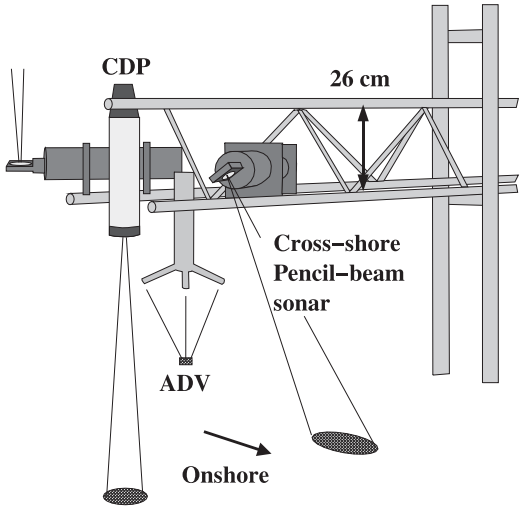

Figure 2. Schematic showing the instrument positions on the mast. The CDP was approximately 80 cm above the bed. Located adjacent to the CDP were an Acoustic Doppler Velocimeter (ADV) and two rotary pencil-beam sonars. The other two support pipes (not shown) are farther to the right.

phase wrapped to a smaller velocity. These ambiguity wraps are removed by adding $\pm 2\pi$ during data processing. The size of the CDP sample volume increases with distance from the transducer due to beam spreading, but typically the sample volume is approximately 4 cm in diameter at a range of 1 m. The vertical thickness of the sample volume is 0.7 cm based on a pulse length of 9.6 μs. Each velocity data point was computed from an average of 24 pulse-pairs. Velocity calibrations of the CDP in a tow-tank indicate an accuracy on the order of 0.5 cm/s over a 1 to 2 m range for a single pulse pair and 1.5-cm range bins [*Zedel et al.*, 1996]. Thus the accuracy of the 24 pulse-pair ensemble is expected to be about 0.1 cm/s. The intensity of the acoustic backscatter from the particles is proportional to the concentration of the suspended sediment. Correlation coefficients provide a measure of data quality and were high even at very low suspended sand concentrations [*Smyth et al.*, 2002]. Thus, in the absence of sand particles in the water column, it is assumed the sound is backscattered from fine sediments. The distance from the transducer to the seafloor is estimated from the CDP backscatter data, and average water depth was estimated from pressure measurements recorded by a pressure sensor on the instrument frame at a rate of 8 Hz.

[17] Data from the cross-shore rotary pencil-beam sonar were used to estimate cross-shore bedform dimensions, and data from a rotary fan-beam sonar were used to aid in the identification of bedform type. Five consecutive rotary sonar images were collected every 10 min during storm conditions, and every half hour otherwise. Ripples were identified visually using fan-beam images at Station C, but in order to ensure that the ripple types were the same at the CDP location, data were used only if the elevation spectra from the pencil-beam data at the CDP location matched those of the offshore location and the ripple type could be unambiguously identified. Bedform height was taken as $2\sqrt{2}$ times the standard deviation of the filtered seafloor elevation for irregular ripples and cross ripples, i.e., assuming a sinusoidal ripple profile. The selected filter bands were 0.5 to 3 cpm for cross ripples and 3 to 10 cpm for irregular ripples. Ripple wavelength for irregular and cross ripples was calculated as

$$\lambda = 2\pi \frac{\sigma_Z}{\sigma_{dZ/dx}}, \tag{12}$$

where σ_Z is the filtered rms elevation and $\sigma_{dZ/dx}$ is the rms of the spatial derivative of the elevation. The linear transition ripples could not be resolved in the pencil-beam data, and wavelength was estimated by finding the peak in radial fan beam amplitude spectra (at Station C). Height was estimated as 3% of the wavelength [*Smyth et al.*, 2002; *Crawford and Hay*, 2001].

[18] A 5-MHz Acoustic Doppler Velocimeter (ADV) collected single-point, 3-component estimates of the particle velocity during the same time interval as the CDP (Figure 3). The ADV was located approximately 15 cm away from the CDP and had a sampling rate of 25 Hz. Throughout the course of the experiment, the distance from the ADV sample volume to the seafloor varied between 45 and 75 cm due to erosion and accretion. These observed bottom depth changes further illustrate one more advantage of remote acoustic profiling systems for bottom boundary layer studies under active sediment transport conditions, particularly for long-term deployments.

[19] Over the entire experiment, 1348 CDP data files were collected. Of these data runs, $\sim$75% were processed and unwrapped. Of the processed data, additional data runs were excluded for the following reasons: (30%) bedform type could not be unambiguously identified, and/or the bedform crests of the linear transition ripples were oriented greater than $\pm 15^\circ$ to shore normal; (17%) no corresponding bedform data; (15%) bedslope was greater than $\pm 0.5^\circ$; (15%) current larger than 20 cm/s; (3.5%) bed was closer than 60 cm to the instrument mast; (2%) data run of the ADV or CDP was less than 15 min; (2%) unusual bottom returns or suspected near-bed biological interference; (2%) no corresponding water depth information. With all of these exclusions, 15% of the unwrapped and processed CDP runs are used in the analysis.

[20] In order to minimize vertical velocities induced by horizontal motion over a sloped bed, only time intervals when bedslopes were less than 0.5 degrees were considered for the high-energy cases (linear transition ripples and flat bed). Bedslope was estimated from the cross-shore elevation profiles collected by the pencil beam sonar at frame B. Bedslopes were estimated over 2 intervals: 1 m centered about the cross-shore pencil-beam transducer coordinate and a more coarsely resolved 3.5-m interval (from 0.5 m onshore of the pencil beam transducer to 2.5 m offshore). In general, average bedslopes estimated from the two nearest CRAB profiles over a 10-m range at the CDP cross-shore location were small: 0.3 $\pm$ 0.6 degrees and 0.8 $\pm$ 0.3 degrees.

3.3. Bedstate and Forcing Time Series

[21] During the experiment, there was a variety of wave conditions including swell, quiescent conditions, and seven storms with wave rms velocities exceeding 0.5 m/s. Figure 3

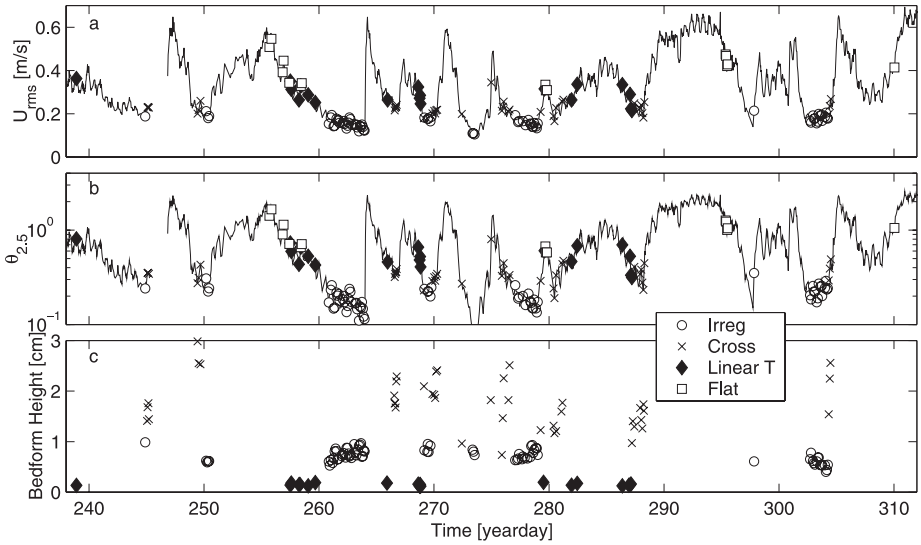

Figure 3. Time series of (a) horizontal rms velocity measured by the Acoustic Doppler Velocimeter (ADV); (b) the grain roughness Shields parameter, $\theta_{2.5}$; and (c) bedform height for the ripple cases. Number of data runs: irregular ripples, 77 (open circles); cross ripples, 43 (crosses); linear transition ripples, 19 (solid diamonds); and flat bed, 16 (open squares).

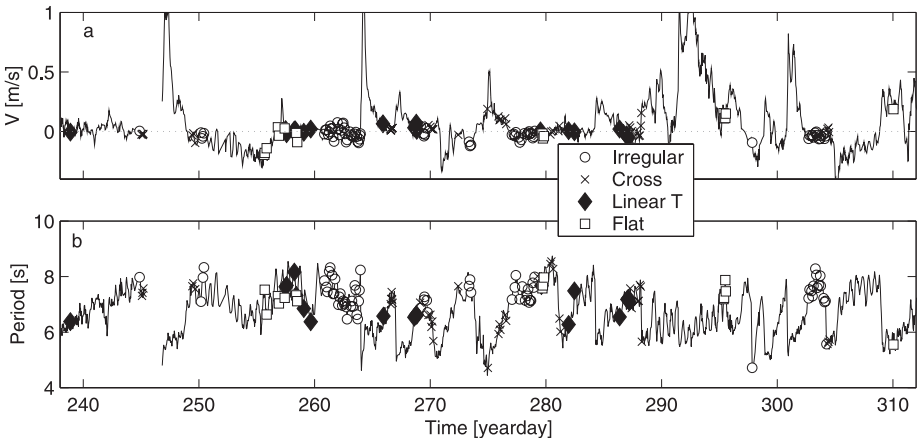

Figure 4. Time series of (a) average longshore current, V, measured by the ADV and (b) energy weighted average incident wave period.

shows a summary of the rms horizontal wave velocity, grain roughness Shields parameter and bedform height over the entire experiment at frame B.

[22] Data runs indicated by the different bedstate symbols in Figure 3 were used in this analysis, as explained later. Bedstate showed a progression with increasing wave energy: irregular ripples at low energies, followed by cross ripples, linear transition ripples and finally flat bed at the highest wave energies [see also *Hay and Wilson*, 1994; *Clifton*, 1976]. Longshore currents occasionally exceeded 1 m/s (Figure 4a).

[23] As our purpose here is to study the wave bottom boundary layer in the absence of currents, only time intervals when the average longshore current was less than 0.2 m/s were considered. As shown in Figure 4b, the energy-weighted incident wave period varied from 4.5 to 9 s over the experiment. The energy-weighted incident wave period was estimated from the integral of the frequency times the velocity spectrum normalized by velocity spectral variance in the frequency band 0.05 to 0.6 Hz (1.7 to 20 s period).

4. Velocity Spectra

4.1. Near-Bed Velocity Spectra

[24] Figure 5 shows the vertical velocity power spectral density (S_{ww}) for the CDP data within the wave bottom boundary layer (z = 3.4 cm). The peak spectral energies in the incident wave band are highest for the lowest energy cases, which is noteworthy as the wave energies in the free-stream for flat bed conditions are larger by a factor of 7 than those for irregular ripples. The source of the energy in the incident wave band for the low-energy cases is likely irrotational vertical motions induced by flow over bedforms [*Davies*, 1983; *Hay et al.*, 1999] and large-scale turbulence associated with vortices shed from ripple crests. The power

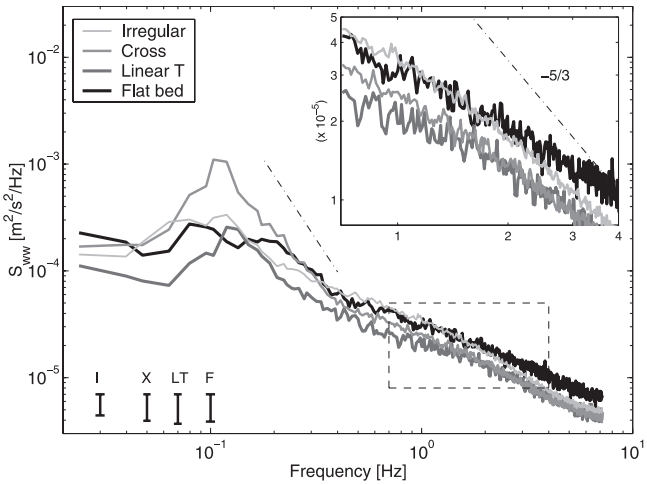

Figure 5. CDP vertical velocity power spectral densities 3.4 cm above the bed. The region indicated by the dashed box is shown enlarged in the inset. Degrees of freedom: irregular ripples, 1850; cross ripples, 982; linear transition ripples, 424; and flat bed, 366. Confidence intervals are shown for the four spectra in the lower left-hand corner.

spectral densities are similar for all bedstates at frequencies above 0.5 Hz, indicating that near-bed turbulence intensity is independent of wave energy. Friction factors based on near-bed maxima in turbulence intensity are estimated in section 6. Spectral slopes in the range $0.7 < f < 4$ Hz are less steep than $-5/3$, and flatten close to the Nyquist frequency. Observations of the wave bottom boundary layer from the earlier field experiment also showed spectral convergence for the four bedstates above 1 Hz, and spectral slopes flatter than $-5/3$ [*Smyth et al.*, 2002].

4.2. Free-Stream Velocity Spectra

[25] Figure 6 shows the horizontal cross-shore velocity power spectral densities (S_{uu}) from the ADV data. The spectra are averaged over 53, 18, 13 and 13 data runs for irregular, cross, linear transition ripples and flat bed, respectively. (These were the data runs for which the CDP profile extended up to the ADV measurement volume.) The power spectral densities in the incident wave band are clearly separated by bedstate with the highest spectral densities occurring for the flat bed case, and decreasing through linear transition ripples, cross ripples to the lowest densities for irregular ripples.

[26] Spectral slopes on the high-frequency side of the incident wave band for S_{uu} range from -3 to slightly steeper than -5. Expected values of the slope are -3 for shallow water waves and -5 for deep water waves [*Thornton*, 1979; *Phillips*, 1966, p. 111]. For a water depth of 3.4 m, frequencies less than 0.11 Hz have a water depth to wavelength ratio less than 0.07 and are classified as shallow water waves [*Kundu*, 1990, p. 203]. Deep water waves occur at frequencies above 0.35, with a water depth to wavelength ratio larger than 0.28. Slopes of S_{uu} in previous nearshore observations range between -3 and -5 [*George et al.*, 1994; *Kosyan et al.*, 1996; *Foster et al.*, 2000].

[27] A slope break in the spectra occurs at approximately 0.5 Hz. Similar slope breaks have also been observed in previous experiments: at ~2 Hz by *George et al.* [1994] at $z = 38$ cm and ~1 Hz by *Foster et al.* [2000] at $z > 4$ cm. The spectral densities above the slope break all have slopes slightly flatter than $-5/3$. A gradual flattening of the spectral slope occurs in the high-frequency tail, suggestive of a noise floor. Noise levels of 7.5×10^{-6}, 7.2×10^{-6}, 8.6×10^{-6}, and 1.7×10^{-5} m^2/s^2/Hz were removed for the four bedstates, respectively. As shown in the inset of Figure 6, with the noise removed, the horizontal velocity spectra have approximately a $-5/3$ slope in the frequency range 0.6 to 10 Hz. The horizontal longshore velocity spectra, S_{vv}, also have a $-5/3$ slope over this frequency range after the removal of noise. Although they are not shown here, the spectral densities averaged over the bedstates for S_{vv} are the same as S_{uu} in the frequency range 0.6 to 10 Hz.

[28] The vertical velocity power spectra (S_{ww}) for both the CDP data and the ADV data at the height of the ADV sample volume are shown in Figure 7. In the incident wave band at frequencies above the peak, the spectral slope is ~ -3. In contrast to the near-bed power spectral densities, the free-stream densities are very different for different bedstates. A slope break is again present at approximately 0.5 Hz, like S_{uu}.

[29] In the incident wave band, the spectra from the two instruments match very closely, particularly for the high-energy cases. At frequencies above 0.5 Hz, spectral densities increase with increasing wave energy and roll off at a slope of approximately $-5/3$. Discrepancies between the ADV and CDP spectra for these frequencies are partially due to temporal aliasing in the CDP processing, which are examined in the next subsection.

4.3. Noise and Aliasing

[30] The ADV is expected to have a higher noise floor in the horizontal velocity spectrum than in the vertical due to transducer configuration. For this particular instrument the transformation matrix provided by the manufacturer (Sontek

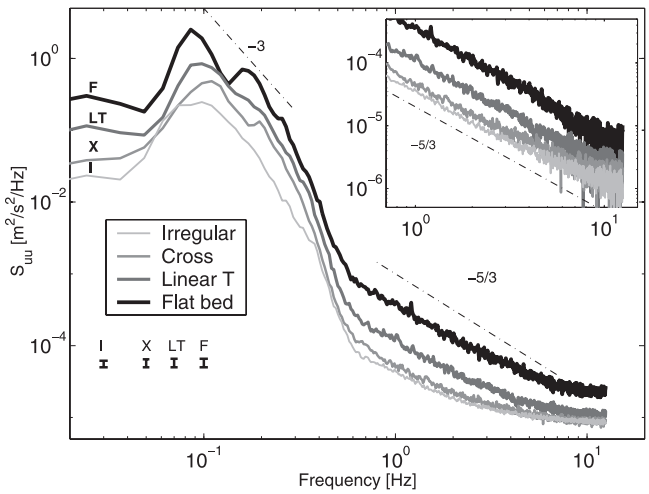

Figure 6. Power spectral densities, S_{uu}, of the ADV horizontal velocity. The 95% confidence intervals are also shown for the averaged spectra with degrees of freedom: (I) irregular ripples, 1802; (X) cross ripples, 612; (LT) linear transition ripples, 442; and (F) flat bed, 442. Dash-dotted lines are -3 and $-5/3$ slopes. In the inset a noise floor has been removed for each S_{uu}.

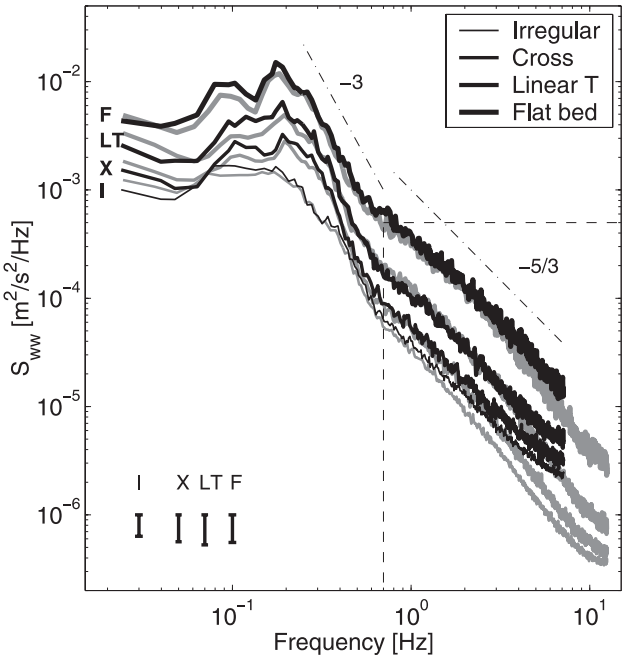

Figure 7. Power spectral densities, S_{ww}, of the ADV (shaded) and CDP (black) vertical velocities at the height of the ADV sample volume. Degrees of freedom for the ADV data are listed in Figure 6. Degrees of freedom for the CDP data: irregular ripples, 1274; cross ripples, 382; linear transition ripples, 280; and flat bed, 294.

probe number 5036) predicts a velocity variance which is 30.8 times higher in S_{uu} than in S_{ww} and 31.2 times higher in S_{vv}. Given a noise floor of 7.5×10^{-6} m^2/s^2/Hz in S_{uu}, the predicted noise floor for S_{ww} is 2.4×10^{-7}.

[31] The coherence and phase of the cross-spectra of the vertical velocity measured by the CDP and ADV, Figure 8, indicate high coherence and small phase differences in the incident wave band. Low coherence is associated with random phases oscillating about zero, and is observed at frequencies above 0.5 Hz. In this frequency range the S_{uu} spectra have a $-5/3$ slope and the turbulence has scales smaller than the physical separation of the instruments. These observations support the use of a 0.7-Hz filter to separate waves from turbulence (section 5).

[32] The high-frequency portion of Figure 7 is enlarged and separated by bedstate in Figure 9. At frequencies near the CDP Nyquist frequency, the spectra differ systematically, with higher levels in the CDP.

[33] A flattening in the high-frequency tail of the CDP spectra is partly due to aliased energy which occurs because of the dead time between pulse bursts [*Zedel and Hay*, 1999]. Immediately after the pulse burst, the CDP processes and averages the collected data before transmitting the next pulse burst. For example, processing 24 pulse-pairs at a pulse interval of 1.5 ms requires 36 ms. At an ensemble sampling rate of 18 Hz, there is 19.6 ms of dead time during the 55.6-ms sampling interval. The sampling rate and pulse interval varied throughout the course of the experiment, and the average dead time for the four bedstates was approximately 18 ms. In order to correct the spectra, aliased energy was estimated by finding the best fit between the measured spectrum and a spectrum composed of a linear spectral slope in log-log space with aliased energy mirrored about the Nyquist frequency. An example of this procedure is shown in Figure 10a. The slope and the energy of the spectrum were varied to optimize the fit to the data. The best fit minimized the squared difference of the measured and constructed spectra for $0.7 < f < 4$ Hz, and also minimized the error in the spectral variance estimate. Average regression correlation coefficients between the measured spectra and the best-fit spectra for $0.7 < f < 4$ Hz are shown in Figure 10b. In general, the regression correlation coefficients are high ($\sim$0.85) above the boundary layer. Near the bed, the regression correlation coefficients are lowest for the high-energy runs.

[34] In addition to the removal of aliased energy, a noise floor representing the system velocity uncertainty was also removed from the spectra. The CDP system has a velocity uncertainty due to electronic noise in the receiver. For a similar CDP system [*Zedel et al.*, 1996] estimated this velocity uncertainty as

$$\sigma_m = \frac{1.4 C_s \sigma_s}{4\pi f \tau_i \sqrt{n}}, \tag{13}$$

where C_s is the speed of sound, 1.4 is an empirically determined scaling constant, σ_s = 0.067 radians is an empirically determined phase uncertainty, f = 1.7 MHz is the transmit frequency, τ_i is the pulse interval and n is the number of pulse-pair averages, 24 for the present measurements. These values give a velocity uncertainty of 0.88 mm/s for a 1.5-ms pulse interval, resulting in a noise level of 2.4×10^{-8} m^2/s^2/Hz. This noise floor was subtracted from the spectra, although the effect is small since it is more than a factor of 10 lower than the lowest spectral densities for the lowest energy (irregular ripple) case.

[35] When corrected for aliasing and electronic phase noise, the high-frequency S_{ww} spectra for the CDP became virtually identical to the ADV for the flat bed (highest energy) case, but the CDP spectral densities remained higher than the ADV for the other bedstates. These

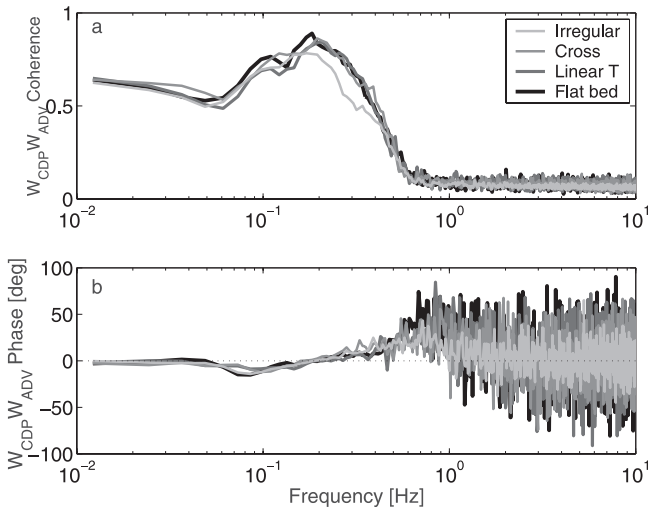

Figure 8. (a) Coherence and (b) phase of the cross-spectra of the CDP and ADV vertical velocities.

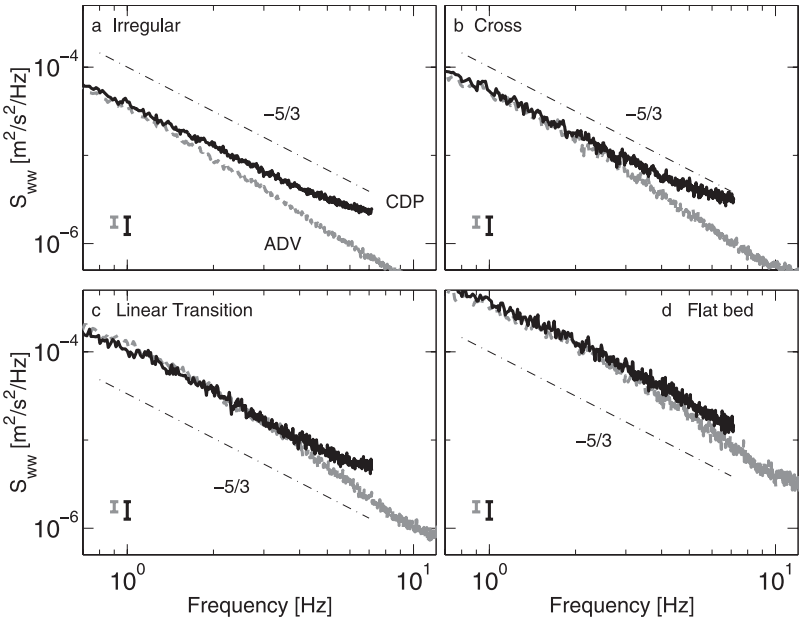

Figure 9. Enlarged view of the boxed region indicated in Figure 7 with spectra separated by bedstate for clarity. Confidence intervals (95%) for the ADV (shaded) and CDP (black) are indicated in the lower left-hand corners.

differences increase at higher frequencies and lower wave energies and are partially due to higher noise levels in the CDP caused by small-scale turbulence, as discussed in Appendix A.

[36] An average noise level of 1.12×10^{-6} (m^2/s^2/Hz) was subtracted from the CDP spectra (Figure 11) and the CDP and ADV spectra are found to overlap. The average noise level was estimated by subtracting the CDP spectral densities from the ADV spectral densities at a frequency of 7.2 Hz. Estimated values were similar for the four bedstates: 8.6×10^{-7}, 13.3×10^{-7}, 1.2×10^{-7} and 1.1×10^{-7} [m^2/s^2/Hz]. These values are close to the noise level of 1.3×10^{-6} [m^2/s^2/Hz] estimated from the measured correlation coefficients (see Appendix A).

[37] Note that above about 3 Hz, the spectral slopes are generally steeper than −5/3. At present, the reason for this effect is unknown. It seems unlikely that it is an instrumental effect, as both the CDP and the ADV have steeper S_{ww} slopes for the high-energy cases despite their very different measurement geometries.

4.4. Spectral Slopes and Isotropy

[38] Spectral slopes were estimated from the spectra (corrected for aliasing and an electronic noise floor as described above) between $0.7 < f < 4$ Hz by fitting a straight line to log S_{ww} versus log f. Vertical profiles of the average spectral slopes for the four bedstates are shown in Figure 12a. At $z = 40$ cm, the slopes range from −1.3 to −1.5, then flatten toward the bed, attaining values of approximately −1.2 at $z = 10$ cm. The slopes show some variation between bedstates with low-energy cases having flatter slopes (less negative values) except within the boundary layer. In the boundary layer the spectral slopes for the high-energy cases are flatter.

[39] Spectral slopes in the wavenumber domain were estimated over short time windows following the method of *George et al.* [1994]. Conversion from frequency to wavenumber by invoking Taylor's hypothesis as in quasi-steady flows is not straightforward for oscillatory flows because of the zero free-stream velocities at flow reversal.

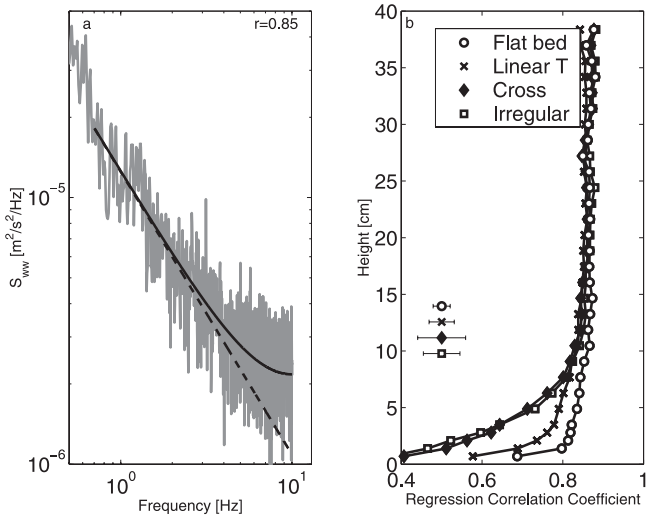

Figure 10. (a) Power spectral densities, S_{ww}, for one CDP data run at the height of the ADV for the irregular ripple case. The dashed line indicates the constant spectral roll-off of the constructed spectrum. The solid black line indicates the power law spectrum aliased at the Nyquist frequency and is the best fit spectrum which also conserved variance over $0.7 < f < 4$ Hz. The regression correlation coefficient for the measured and constructed spectrum was 0.85. (b) Profiles of the average regression correlation coefficient for the four bedstates. The error bars shown separated from the curves represent 5 times the standard error at the indicated height.

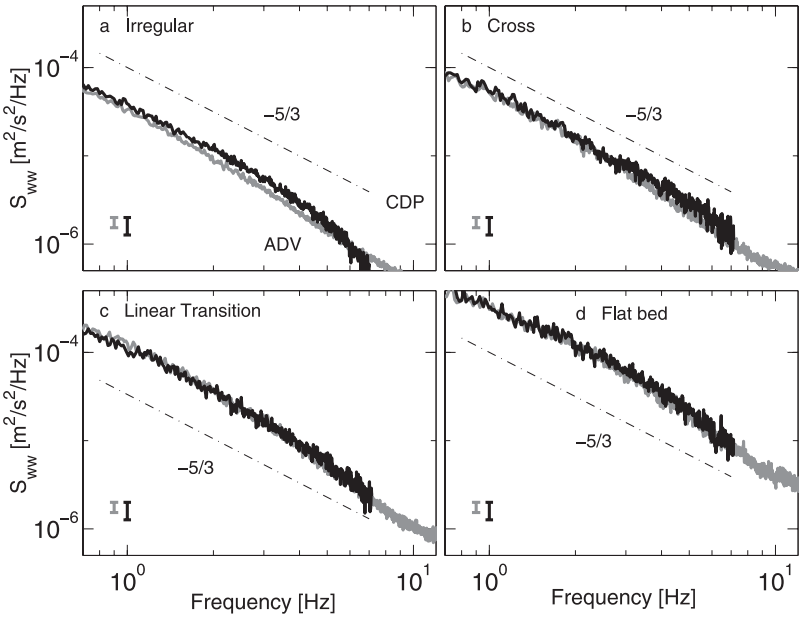

Figure 11. De-aliased power spectral densities, S_{ww}: ADV (shaded) and CDP (black) at the height of the ADV sample volume.

Selected short 16-point time windows (∼1 s) were centered about the crests of the largest half of the waves in a data run. Conversion to wavenumber from frequency used Taylor's hypothesis with the advection velocity taken as the horizontal velocity (measured by the ADV) averaged over the time window. Within the boundary layer, spectral slopes are not estimated as the advection velocity is unknown. The average spectral slope was estimated for each data run, excluding those waves for which the turbulence intensity (based on the high-pass filtered vertical velocity with a 0.7-Hz cutoff) was greater than 20% of the advection velocity, or the regression correlation coefficient of the slope fit was less than 0.5, or the maximum wavenumber exceeded 220 m^{-1} [*Zedel and Hay*, 1999]. The restriction on turbulence intensity excluded 20% of the data for irregular ripples, and ∼5% of the data for the other cases. The restriction on the regression correlation coefficient excluded ∼20% of the data at z = 40 cm. The restriction on the wavenumbers had little effect on the high-energy cases, but excluded a further 15 to 20 percent of the data for the irregular ripples. Spectral slope profiles averaged for the four bedstates are shown in Figure 12b. Estimated spectral slopes range from −1.8 to −1.4 at z = 40 cm followed by a nearly linear trend to flatter slopes toward the bed. Consistent with the slope profiles estimated in frequency space, the spectral slopes are steeper for the higher energy cases above z > 10 cm and flatter below.

[40] Previous measurements of the frequency domain spectral slopes in the wave bottom boundary layer have found that the slope of S_{uu} in the inertial subrange was approximately −5/3 and that the slope of S_{ww} was flatter than −5/3. *Foster et al.* [2000] and *Conley and Inman* [1992] observed a −5/3 slope for S_{uu} in the inertial subrange for measurements in the nearshore zone at heights 0.3 cm to 13.8 cm. Spectral slopes were estimated by *Sleath* [1987] and *Hino et al.* [1983] in the laboratory using laser Doppler anemometers in oscillating-flow tunnels. In the experiment by *Sleath* [1987], measurements were made at z = 0.4 cm over a pebbled surface (D = 3 cm). The slopes of S_{uu} over ∼15° of wave-phase during a half-wave cycle were found to be slightly steeper when the turbulence intensity was high. However, all slopes estimated over the half wave-cycle were approximately −5/3. In the experiment by *Hino et al.* [1983], the tunnel floor was smooth and spectral slopes were estimated at z = 0.5 cm over a 0.2-s window in the acceleration phase and deceleration phase of a half wave-cycle. During the deceleration phase when the turbulence intensity was high, the slope of S_{uu} was approximately −5/3

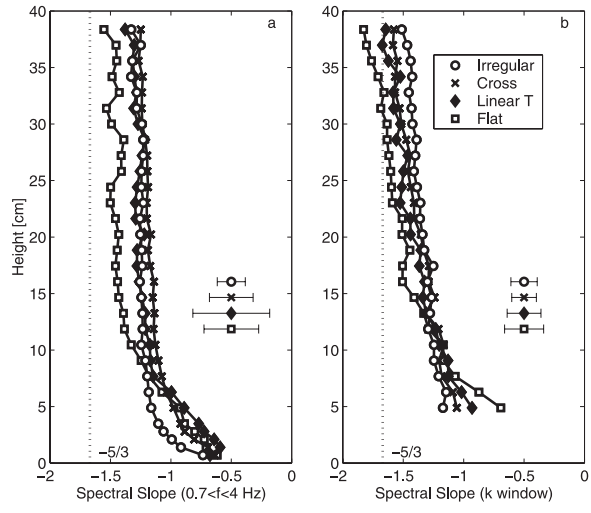

Figure 12. (a) Spectral slopes estimated over a frequency range of 0.7 < f < 4 Hz for the four bedstates. (b) Spectral slopes estimated in wavenumber space with a ∼1-s window about the wave crest. Error bars representing 2 times the standard error at z = 16 cm are plotted beside the slope profiles for clarity. The vertical dotted line indicates a −5/3 slope.

over $20 < f < 100$ Hz, followed by a steeper roll-off at $f > 150$ Hz. The vertical velocity spectrum was also measured in the experiment by *Hino et al.* [1983]. The magnitude of S_{ww} was found to be smaller: approximately a factor of 10 lower at $f = 5$ Hz, slowly merging with S_{uu} at $f > 100$ Hz. In the frequency range where the horizontal velocity spectrum had an approximate $-5/3$ slope, the S_{ww} slope was much flatter, ~ -0.8.

[41] As there are few other comparable data sets for oscillatory boundary layers, the present estimates of spectral slopes and corresponding turbulence anisotropy are compared to quasi-steady shear flow results. Estimates of the slope of S_{ww} can be compared to steady flow results by *Sreenivasan* [1996], who compiled a variety of reported shear flow measurements, including pipe flow, mixing layers, channel flow, jets and boundary layer flows. *Sreenivasan* [1996] found the spectral slope of the normal velocity component to be a slowly varying function of microscale Reynolds number. The normal component is defined in the direction of the highest velocity gradient, orthogonal to the streamwise component and to the wall in the case of a boundary layer flow. The microscale Reynolds number is defined as

$$R_\lambda = \frac{u'\lambda_T}{\nu}, \tag{14}$$

where u' is the turbulent rms velocity, λ_T is the Taylor microscale, and ν is the kinematic viscosity. For microscale Reynolds numbers between 230 and 600, the spectral slope of the normal velocity component was found to be between -1.4 and -1.58, although the spectral slope of the streamwise velocity component was $-5/3$. *Sreenivasan* [1996] suggested the presence of a $-5/3$ slope in the streamwise spectrum was related to large-scale overturning which is suppressed in the normal direction. For the normal velocity component, the absence of energy at low wavenumbers decreases the range of wavenumbers in the inertial subrange. Thus a $-5/3$ slope is found in the normal velocity component only if the microscale Reynolds number is large enough to support a wide inertial subrange.

[42] For the present measurements the microscale Reynolds number at the height of the boundary layer ($\sim$5 cm) was estimated to be approximately 175, as described below. Assuming that there is an approximate balance between the rates of turbulent energy production and dissipation and further assuming that the small-scale turbulence is isotropic at the smallest scales (consistent with the measurements of *Hino et al.* [1983] of S_{uu} and S_{ww}), then the production and dissipation terms may be written in terms of simplified velocity and length scales [*Tennekes and Lumley*, 1972, p. 66]. For the production,

$$-\overline{u_i u_j} S_{ij} \sim u_s^2 \frac{u_s}{\ell}, \tag{15}$$

where the Reynolds stress, $-\overline{u_i u_j}$, is $O(u_s^2)$, and the mean strain rate tensor S_{ij} is $O(u_s/\ell)$, u_s being the velocity fluctuation scale, and ℓ is an integral length scale. For the dissipation, in isotropic turbulence,

$$2\nu\overline{s_{ij}s_{ij}} = 15\nu\overline{(\partial u_1/\partial x_1)^2} \sim \frac{15\nu u_s^2}{\lambda_T^2}, \tag{16}$$

where the fluctuating strain rate product $\overline{s_{ij}s_{ij}}$ is given approximately by ${u_s}^2/{\lambda_T}^2$. These approximations give

$$\lambda_T^2 = \frac{15\nu\ell}{A u_s}, \tag{17}$$

where the constant A is taken to be O(1). Substituting for measured values: $\ell = 5$ cm, $u_s \sim u_* = 4$ cm/s (see section 5) gives $\lambda_T \sim 0.4$ cm and $R_\lambda \sim 175$. On the basis of the steady flow results quoted by *Sreenivasan* [1996] the spectral slope in the vertical power spectral densities would be expected to be between approximately -1.4 and -1.3 at the height of the boundary layer, close to the observed values.

[43] Within the boundary layer the microscale Reynolds number would be expected to vary as

$$R_\lambda = \frac{\lambda_T^2}{\nu}\frac{u_s}{\lambda_T} \propto \frac{\ell}{u_s}\frac{u_s}{\lambda_T}, \tag{18}$$

based on the above scaling arguments. If the Taylor microscale varies as $r_p\sqrt{\nu/zu_*}$ (the case for turbulent pipe flow, where r_p is the radius of the pipe [*Lawn*, 1971]) and the integral length scale is proportional to the height, then within the boundary layer,

$$R_\lambda \sim \left(\frac{z}{u_s}\right)\left(\frac{u_s z^{1/2} u_*^{1/2}}{r\nu^{1/2}}\right) \propto z^{3/2}, \tag{19}$$

where r is an outer length scale. Thus, as z decreases, the microscale Reynolds number is expected to decrease, with a consequent flattening of the spectral slope, consistent with the observations.

[44] In the atmospheric boundary layer, *Kaimal et al.* [1972] found for neutral conditions that the slope of S_{ww} versus dimensionless frequency, fu/z, ceased to be $-5/3$ below a cutoff dimensionless frequency of 1. Laboratory measurements are consistent with these observations, giving dimensionless cutoff frequencies between 1 and 2 [*Saddoughi and Veeravalli*, 1994]. For the present experiment, at a height 6 cm and an advection velocity of 32 cm/s, and an assumed nondimensional cutoff frequency of 1 to 2, the expected cutoff frequency of the $-5/3$ range S_{ww} is 5.3 to 10.7 Hz. This predicted cutoff frequency is close to the Nyquist frequency, and consequently a $-5/3$ slope would not be predicted close to the bed for all bedstates, consistent with our results.

5. Turbulence Intensity Profiles

[45] The objective of this section, quantifying the turbulence intensities for the different bedstates, necessitates separating the waves from the turbulence. There is no generally accepted method of velocity decomposition for the irregular waves and variable bedform geometries typical of nearshore field conditions. In this study, two different decomposition methods are used, one which is expected to underestimate, and the other to overestimate the turbulence intensity, therefore giving a range of values which should encompass the actual turbulence intensity.

[46] The first method of decomposition uses a high−pass filter, separating the turbulent from wave velocities with a

1-Hz cutoff. In the second method, the wave velocity is removed by calculating the wave velocity at all heights using linear wave theory, and defining the turbulent velocity as the residual. Since in the filter method the cutoff frequency is higher than the incident wave peak frequency in the vertical velocity spectra, much of the incident wave band energy is removed from the turbulent velocity. However, the filter method underestimates the amount of turbulence present as filtering removes any turbulent energy which might occur at wave frequencies. The linear wave theory method overestimates the turbulent energy as energy from nonlinear wave interactions, and irrotational vertical motions induced by flow over bedforms [*Davies*, 1983; *Hay et al.*, 1999] are included in the turbulence estimate.

[47] For the filter method, a fifth-order high-pass Butterworth filter was used which had a magnitude response of approximately −100 dB at 0.07 Hz. The cutoff frequency for the filter method was chosen at 0.7 Hz, conservatively higher than the free stream slope break frequency, 0.5 Hz. This method has been used by others with similar cutoff frequencies: 0.8 Hz [*Kosyan et al.*, 1996] and 1 Hz [*Foster et al.*, 2000].

[48] In the second method, the wave velocity was calculated using linear inviscid wave theory. Measured horizontal velocities at the ADV height were used to determine the vertical wave velocity, $\tilde{w}$,

$$\tilde{w} = \frac{\tanh kz}{\omega} \frac{\partial \tilde{u}}{\partial t}, \tag{20}$$

where z is the height above bottom, $\tilde{u}$ is the low-pass filtered horizontal velocity (fifth-order Butterworth filter with a 1-Hz cutoff) and k is the wavenumber obtained from the dispersion relation,

$$\omega^2 = gk \tanh kh, \tag{21}$$

where h is the water depth. Wave velocities were estimated spectrally for wave periods between 2 and 20 s.

[49] Profiles of the turbulent rms vertical velocity (Figure 13) indicate the turbulence intensity near the bed is similar for all bedstates, as expected from the spectral convergence within the inertial subrange at $z = 3.4$ cm in Figure 5. Also as expected, the turbulence intensity is lower for the filter method, approximately 30 to 40% lower near the bed ($z <$ 5 cm) for the low-energy cases and 20 to 25% lower for the high-energy cases. Between $z = 5$ and 10 cm, the low-energy cases remain approximately 30% to 40% lower, but the reduction ranges from 25 to 35% for the high-energy cases.

[50] A similar slow decay of the w'_{rms} profile with distance from the bed is found in the measurements of *Jensen et al.* [1989], which were made over smooth and rough beds in an oscillatory water tunnel. The half-cycle averaged w'_{rms} profiles for their runs 12 and 13, with 350-micron diameter fixed sand grain roughness, exhibit decreases of about 50% and 30% respectively over 15 cm height (midway between the top and bottom of the tunnel). The oscillation period for these runs was 9.7 s, and the oscillation velocity amplitudes were 1 and 2 m/s respectively, values roughly comparable to our higher energy, linear transition ripple and flat bed cases. Jensen et al. also made measurements for the same forcing conditions but with smooth beds (their runs 8 and 10). The w'_{rms} profiles for the smooth bed runs indicate similar turbulence levels at a height of 15 cm to the respective rough bed runs. The most likely source of the turbulence above the boundary layer was considered to be the contraction sections in the tunnel during flow reversal [*Jensen et al.*, 1989, p. 28]. The comparable turbulence levels at mid-depth in the tank, for smooth and rough bed runs with the same forcing parameters, suggest that the turbulence due the sand-roughness decayed to near zero levels at heights of O(10 cm), or about twice δ, the latter being taken from Jensen et al.'s Figure 34. It seems likely to us that the slow decay of turbulence levels with height evident in our data (especially for the higher wave energy bed states) is similarly due to sources of turbulence other than the wave-induced shear at the bed. In our case, these sources include surface-injected turbulence (i.e., wave breaking) and turbulence associated with mean flows (e.g., the longshore current), both of which are likely to be more important as wave energy increases. Note that even though the data presented here are for weak longshore currents, the mean flow Reynolds number is still large: O(10^6) for 20 cm/s flows. Eddy shedding from the instrument, which is known to produce significant flow disturbance [*Zedel and Hay*, 2002], or from the cantilevered mast and support frame, are also possible sources of turbulence.

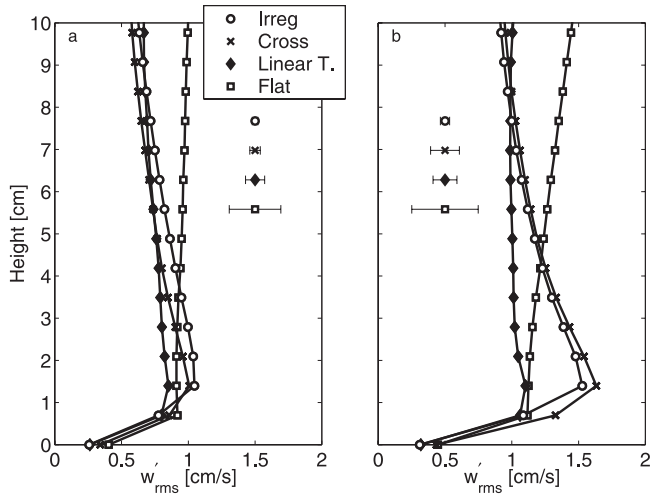

Figure 13. Profiles of the rms vertical turbulent velocity calculated by (a) the filter method and (b) the linear wave theory method. Representative error bars for 7.5 cm height, displaced from the plotted points for clarity, are twice the standard error.

[51] The *Jensen et al.* [1989] data are also of interest in relation to the height above bed of the peak turbulence intensity. Taking their smooth bed runs into account, a peak is clearly visible in the half-cycle averaged w'_{rms} profile for run 13, and is at a height of about 0.32δ. In our data, the peak occurs at comparable heights: at 0.17δ when the bed was flat, and 0.37δ when linear transition ripples were present.

6. Friction Velocities and Wave Friction Factors

[52] In this section, measured values of the peak near-bed turbulence intensity are used to estimate the wave friction factor. It is assumed that $w'_{rms} = u_*/2$, based on the following experimental evidence. Observations by van Doorn (given by *Nielsen* [1992, p. 72]) for oscillatory flow over fixed

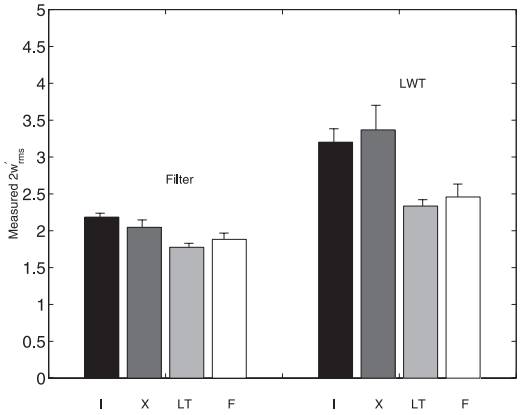

Figure 14. Measured values of $2w'_{rms}$ at the near-bed peak in the w'_{rms} profiles for the four bedstates: I, irregular ripples; X, cross ripples; L, linear transition ripples; and F, flat bed. Error bars identify 2 times the standard error about the mean.

roughness elements found the ratio of w'_{rms} (at the height of the roughness elements) to u_* was approximately 0.5. Measurements by *Sleath* [1987] in an oscillatory flow tunnel with regular waves and a sandpaper bed ($d = 1.63$ mm) found w'_{rms}/u_* was approximately 0.57, where w'_{rms} was taken as the near-bed peak in turbulence intensity, and the friction velocity was defined in terms of the velocity defect relation, equation (2). Measurements by *Jensen et al.* [1989] in an oscillatory flow tunnel with regular waves found that w'_{rms}/u_* was 0.7 for a smooth bed (their run 10) and 0.53 for a sandpaper bed (their run 13), where u_* was obtained by fitting the horizontal velocity to a logarithmic wall layer.

[53] Figure 14 shows the measured peak near-bed ensemble-averaged vertical turbulence intensity. Near-bed peak turbulence intensities were found by locating the maximum in the measured turbulence intensity profile between z = 0.69 and 3.5 cm. In general, there was a near-bed peak within this region, but for some data runs the turbulence intensity was higher at 3.5 cm than at the near-bed peak. In these cases, the position of the maximum gradient in turbulence intensity was found (usually the sample bin immediately above the bed), and the value of the turbulence intensity at this position was used. Instances where the turbulence intensity increased monotonically from the bed were not used. Values of u_* are listed in Table 1 along with the boundary layer thickness, δ, estimated as u_*/ω.

[54] Wave friction factors were estimated using equations 3 and 4, giving

$$f_w = 2\left(\frac{\overline{2w'_{1/3}}}{\overline{u_{1/3}}}\right)^2, \qquad (22)$$

where the overbar indicates an ensemble average over all runs for a given bedstate, and using the assumption $u_* = 2w'_{1/3}$. Figure 15 presents the observed wave friction factors plotted relative to grain roughness Shields parameter, θ_d, calculated using $k_N = d_{50}$ in equation (6), rather than $\theta_{2.5}$ in order to facilitate comparison to work by *Tolman* [1994]. Two estimates are given, one for each method of velocity decomposition. Measured wave friction factors vary from $\sim$0.2 for irregular ripples to 0.01 for flat bed conditions (Table 1). Also shown in Figure 15 are predicted wave friction factors from *Swart* [1974], *Tolman* [1994], and *Grant and Madsen* [1982]. Wave friction factors from *Swart* [1974] (equation (10)) were modified by *Nielsen* [1992, p. 159] to include ripple roughness and a contribution from moving grains in the roughness parameter (equation (11)). Wave friction factors predicted by *Grant and Madsen* [1982] overestimate the measured values, but those from *Tolman* [1994] are generally consistent with the measurements. A critical Shields parameter of 0.059 gave the best fit to the data. For the low-energy bedstates, the predictions from *Swart* [1974] and *Nielsen* [1992] underestimate the measured friction factors.

Table 1. Measured Friction Velocity, u_*, Estimates for the Four Bedstates as Well as Boundary Layer Thickness, δ, Estimated Using the Filter Method, Significant Horizontal Velocity, $u_{1/3}$, Ripple Height, η, Ripple Wavelength, λ, Mean Water Depth, h, and Friction Factor Estimates

Bedstate	I	X	LT	F
u_*, cm/s	4.1	3.9	3.4	3.7
δ, cm	4.8	4.2	3.8	4.2
$u_{1/3}$, cm/s	32	45	58	82
η, cm	0.72	1.78	0.45	–
λ, cm	18	75	8.9	–
h, m	3.4	3.5	3.5	3.4
f_w (filter)	0.037	0.017	0.0075	0.0042
f_w (LWT)	0.079	0.045	0.013	0.0072

7. Summary and Conclusions

[55] Measurements of vertical velocity within and above turbulent oscillatory wave boundary layers have been inves-

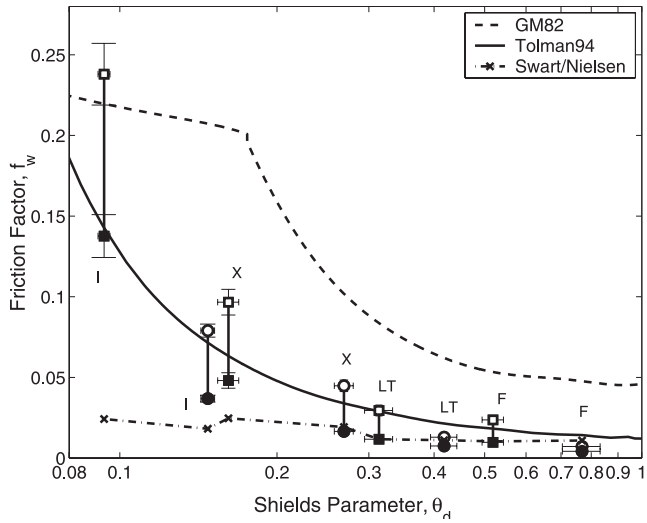

Figure 15. Wave friction factor as a function of grain roughness Shields parameter. Measured values for each bedstate are for the linear wave theory decomposition method (open symbols) and the filter velocity decomposition method (solid symbols). Error bars indicate the standard error about the mean. Results from a previous field experiment [*Smyth et al.*, 2002] are indicated by square symbols. Dashed, solid and dash-dotted lines are predictions of the wave friction factor from *Grant and Madsen* [1982], *Tolman* [1994], and *Swart* [1974] and *Nielsen* [1992, p. 159], respectively.

tigated for different bedstates in the nearshore. Above the boundary layer, power spectral densities of the ADV vertical velocity have a slope break at approximately 0.5 Hz, separating a steep roll-off (−3 to −5) for lower frequencies from an approximate −5/3 slope for higher frequencies. The cross-spectra of the ADV and CDP vertical velocity also change at this frequency, exhibiting a drop in coherence and a switch from slowly varying phases near zero to large random phases for higher frequencies. These observations indicate the presence of inertial subrange turbulence for frequencies above 0.5 Hz. Turbulence intensities increased on average with ensemble-averaged wave energies.

[56] Within the boundary layer the spectral characteristics differ from the those of the free-stream. Below 0.5 Hz the peak spectral densities are highest for low-energy conditions, and above 0.5 Hz the spectral densities converge. Spectral slopes are flatter than −5/3 for frequencies above 0.5 Hz, and a slope break is not always present. As the bed is approached, the slopes of vertical velocity power spectra become progressively less steep, reaching values between −1/2 and −1 at the bed. These relatively flat spectral slopes suggest the inertial subrange turbulence is anisotropic, an observation consistent with laboratory turbulence spectra which show a similarly reduced spectral roll-off for the transverse velocity component at microscale Reynolds numbers below 1000 [*Sreenivasan*, 1996].

[57] The magnitude of the near-bed peak in the ensemble-averaged turbulence intensity is similar for all bedstates, a result consistent with the observation of spectral convergence in the inertial subrange. A constant level of near-bed turbulence intensity for all of the bedstates, despite the large change in average wave energy, results from differences in the physical roughness due to the active adjustment of the mobile bed in producing different bedstates. Estimated wave friction factors are highest for the irregular ripples at approximately 0.2, while high-energy cases (small amplitude ripples and flat bed) have smaller friction factors, approximately 0.01. Friction factor predictions from *Tolman* [1994] which include mobile bed roughness parameterizations for irregular waves from *Madsen et al.* [1990] are able to predict the general trend of the measurements.

Appendix A: Comparison of ADV and CDP Noise Levels

[58] Turbulence intensities for both methods of velocity decomposition may be larger than expected due to the presence of noise in the CDP system. As noted in section 4, spectral densities for the CDP are higher than the ADV at high frequencies, even though corrections for aliasing and electronic noise were applied to the CDP data (Figure 11). In this section the magnitude of the nonelectronic noise variance is estimated for the CDP data.

[59] Defining σ_p as the velocity uncertainty due to noise other than electronic noise, then the squared correlation coefficient, R^2 is given by

$$R^2 = \exp\left(-8\pi^2\tau_i^2 f^2\left(\sigma_p^2 + \sigma_m^2\right)/C_s^2\right), \tag{A1}$$

where C_s is the speed of sound, σ_m is the velocity uncertainty associated with the electronics (equation (13)), σ_p is the velocity uncertainty associated with phase noise

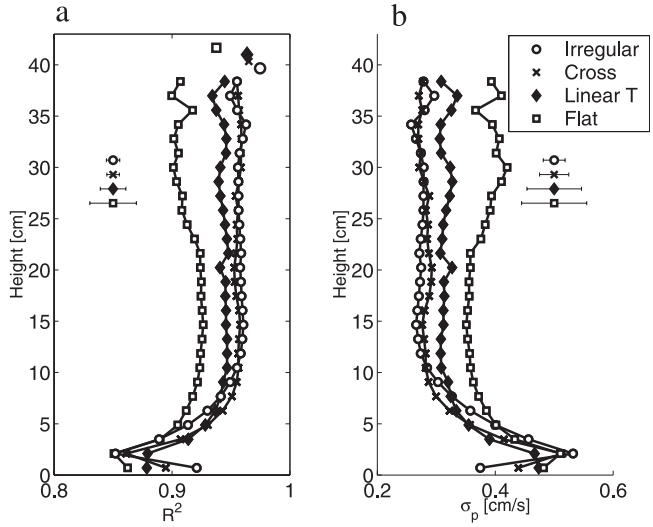

Figure A1. (a) Average squared correlation coefficient of the vertical velocity for the CDP (lines) and ADV (symbols near z = 40 cm). (b) Predicted noise levels for the CDP data based on equation (A1). Error bars in Figures A1a and A1b represent 3 times the standard error.

other than electronic, f is the transmit frequency, and τ_i is the pulse interval. Average squared correlation coefficients from the CDP and ADV are shown in Figure A1, along with the estimated velocity uncertainties for the CDP. Squared correlation coefficients are a few percent lower for the CDP, supporting the idea that the CDP has a higher noise level than the ADV. Estimated velocity uncertainties range from 0.3 to 0.4 cm/s in the free stream, approximately 4 to 5 times the electronic noise velocity uncertainty. A 0.3 cm/s velocity uncertainty corresponds to a spectral level of approximately 1.3×10^{-6} m^2/s^2/Hz, about 75% of the lowest energy level for the irregular ripples at the height of the ADV. Estimated velocity uncertainties are larger near the bed, approaching 0.5 cm/s.

[60] Velocity variance due to the noise in the CDP data may be due to particle exchange in the sample volume, strong velocity shear in the sample volume, and relative motions among the particles in the sample volume caused by small-scale turbulence. The ratio of the noise variance for the ADV and CDP may be estimated using the parameterizations given by *Voulgaris and Trowbridge* [1998]. For Doppler broadening noise, the ratio of the velocity variance is given by

$$\frac{\sigma_D^2|_1}{\sigma_D^2|_2} = \frac{B_1 f_2^2 n_2 \tau_{p2}}{B_2 f_1^2 n_1 \tau_{p1}} = 2.9\frac{B_1}{B_2}, \tag{A2}$$

where B is the spectral broadening, subscripts 1 and 2 indicate the CDP and ADV, respectively, and system parameters are as listed in Table A1. Noise due to small-scale turbulence results in a spectral broadening of

$$B = 2.4\frac{(f\epsilon d)^{1/3}}{C_s}, \tag{A3}$$

where ϵ is the turbulence dissipation rate, and d is the scale of the sample volume [*Cabrera et al.*, 1987]. The ratio of the velocity variance for turbulence-induced spectral broadening is 1.34, indicating the CDP velocities will be noisier

Table A1. System Parameters for the ADV and CDP[a]

Parameter	ADV	CDP
System frequency, f	5 MHz	1.7 MHz
Number of pulse-pairs, n	~58	24
Pulse interval, τ_i	0.208 ms	~1.5 ms
Sample volume width, d_u	1.2 cm	~3 cm
Sample volume height, d_w	1.8 cm	0.69 cm

[a]The pulse interval for the ADV is an average of three pulse intervals of 0.096, 0.176, and 0.352 ms.

than the ADV for the same level of turbulence. Dividing the velocity uncertainty by the square root of this ratio results in an expected noise floor of 1.3×10^{-7} m^2/s^2/Hz.

[61] In summary, higher noise predictions caused by small-scale turbulence are consistent with the observations of noise indicated by the flattening of the high-frequency tail in the S_{ww} and lower correlation coefficients for the CDP data.

[62] **Acknowledgments.** The authors wish to thank W. Birkemeier and the staff of the Army Corps of Engineers Field Research Facility for their cooperation and support, without which this research would not have been possible. We are particularly grateful to L. Zedel (Memorial University of Newfoundland) for his work on the development of the CDP, and for valuable discussions related to Doppler processing. We also thank R. Craig and W. Paul for their very capable technical support, T. Mudge for processing the rotary sonar data, and the graduate students and other staff members from Dalhousie and Memorial who participated in SandyDuck97. Thanks also to Mutlu Sumer for providing the authors with phase-averaged turbulence profiles. We are thankful for the constructive remarks of the two anonymous reviewers. This work was funded by the U.S. Office of Naval Research Coastal Sciences Program, and the Natural Sciences and Engineering Research Council of Canada.

References

Abramowitz, M., and I. A. Stegun, *Handbook of Mathematical Functions*, Dover, New York, 1965.

Cabrera, R., K. Deines, B. Brumley, and E. Terray, Development of a practical coherent acoustic Doppler current profiler, *IEEE J. Oceanic Eng.*, *87*, 93–97, 1987.

Clifton, H., Wave-formed sedimentary structures-A conceptual model, in *Beach and Nearshore Sedimentation*, edited by R. Davis and R. Ethington, *SEPM Spec. Publ.*, *24*, 126–148, 1976.

Conley, D. C., and D. L. Inman, Field observations of the fluid-granular boundary layer under near-breaking waves, *J. Geophys. Res.*, *97*, 9631–9643, 1992.

Crawford, A. M., and A. E. Hay, Linear transition ripple migration and wave orbital velocity skewness: Observations, *J. Geophys. Res.*, *106*, 14,113–14,128, 2001.

Davies, A. G., Wave interactions with rippled sand beds, in *Physical Oceanography of Coastal and Shelf Seas*, chap. 1, pp. 1–62, Elsevier, New York, 1983.

Foster, D. L., R. A. Beach, and R. A. Holman, Field observations of the wave bottom boundary layer, *J. Geophys. Res.*, *105*, 19,631–19,647, 2000.

George, R., R. E. Flick, and R. T. Guza, Observations of turbulence in the surf zone, *J. Geophys. Res.*, *99*, 801–810, 1994.

Grant, W. D., and O. S. Madsen, Movable bed roughness in unsteady oscillatory flow, *J. Geophys. Res.*, *87*, 469–481, 1982.

Hay, A. E., and D. J. Wilson, Rotary sidescan images of nearshore bedform evolution during a storm, *Mar. Geol.*, *119*(1), 57–67, 1994.

Hay, A. E., C. Smyth, L. Zedel, and T. Mudge, On remotely probing the structure of the bottom boundary layer over an evolving sea bed, in *Coastal Ocean Processes Symposium: A Tribute to William D. Grant*, *Rep. 99-04*, pp. 99–106, Woods Hole Oceanogr. Inst., Woods Hole, Mass., 1999.

Hino, M., M. Kashiwayanagi, A. Nakayama, and T. Hara, Experiments on the turbulence statistics and the structure of a reciprocating oscillatory flow, *J. Fluid Mech.*, *131*, 363–400, 1983.

Jensen, B. L., B. M. Sumer, and J. Fredsoe, Turbulent oscillatory boundary layers at high Reynolds numbers, *J. Fluid Mech.*, *206*, 265–297, 1989.

Jonsson, I. G., Wave boundary layers and friction factors, paper presented at 10th International Conference on Coastal Engineering, Am. Soc. of Civ. Eng., Tokyo, 1966.

Kaimal, J. C., J. C. Wyngaard, Y. Izumi, and O. R. Cote, Spectral characteristics of surface-layer turbulence, *Q. J. R. Meteorol. Soc.*, *98*, 563–589, 1972.

Kosyan, R. D., H. Kunz, S. Y. Kuznetsov, and M. V. Krylenko, Sand suspension events and intermittency of turbulence in the surf zone, paper presented at 26th International Conference on Coastal Engineering, Am. Soc. of Civ. Eng., Orlando, Fla., 1996.

Kundu, P. K., *Fluid Dynamics*, Academic, San Diego, Calif., 1990.

Lawn, C. J., The determination of the rate of dissipation in turbulent pipe flow, *J. Fluid Mech.*, *48*, 477–505, 1971.

Madsen, O S., P. P. Mathiesen, and M. M. Rosengus, Movable bed friction factors for spectral waves, paper presented at 22nd International Conference on Coastal Engineering, Am. Soc. of Civ. Eng., Delft, Netherlands, 1990.

Ngusaru, A. S., Cross-shore migration of lunate mega-ripples and bedload sediment transport models, Ph.D. thesis, Memorial Univ., St. John's, Newfoundland, Canada, 2000.

Nielsen, P., *Coastal Bottom Boundary Layers and Sediment Transport*, 324 pp., World Sci., River Edge, N. J., 1992.

Phillips, O. M., *The Dynamics of the Upper Ocean*, Cambridge Univ. Press, New York, 1966.

Saddoughi, S. G., and S. V. Veeravalli, Local isotropy in turbulent boundary layers at high Reynolds number, *J. Fluid Mech.*, *268*, 333–372, 1994.

Sleath, J. F. A., Turbulent oscillatory flow over rough beds, *J. Fluid Mech.*, *182*, 369–409, 1987.

Smyth, C., A. E. Hay, and L. Zedel, Coherent Doppler Profiler measurements of near-bed suspended sediment fluxes and the influence of bedforms, *J. Geophys. Res.*, *107*, 3105, 10.1029/2000JC000760, 2002.

Sreenivasan, K. R., The passive scalar spectrum and the Obukhov-Corrsin constant, *Phys. Fluids*, *8*, 189–196, 1996.

Swart, D. H., Offshore sediment transport and equilibrium beach profiles, *Rep. 131*, Delft Hydraul. Lab., Delft, Netherlands, 1974.

Tennekes, H., and J. L. Lumley, *A First Course in Turbulence*, 300 pp., MIT Press, Cambridge, Mass., 1972.

Thornton, E. B., Energetics of breaking waves within the surf zone, *J. Geophys. Res.*, *84*, 4931–4938, 1979.

Thornton, E. B., and R. Guza, Transformation of wave height distribution, *J. Geophys. Res.*, *88*, 5925–5938, 1983.

Tolman, H. L., Wind waves and movable-bed bottom friction, *J. Phys. Oceanogr.*, *24*, 994–1009, 1994.

Trowbridge, J. H., and Y. C. Agrawal, Glimpses of a wave boundary layer, *J. Geophys. Res.*, *100*, 20,729–20,745, 1995.

Voulgaris, G., and J. H. Trowbridge, Evaluation of the Acoustic Doppler Velocimeter (ADV) for turbulence measurements, *J. Atmos. Oceanic Technol.*, *15*, 272–289, 1998.

Wilson, D. J., and A. E. Hay, High resolution sidescan sonar observations of small scale sand bedforms under waves: A comparison of field and laboratory measurements, report, 16 pp., Memorial Univ., St. John's, Newfoundland, Canada, 1995.

Wilson, K. C., Friction of wave-induced sheet flow, *Coastal Eng.*, *12*, 371–379, 1989.

Zedel, L., and A. E. Hay, Coherent Doppler sonar: Sediment flux and turbulent velocities in a wave flume, paper presented at 26th International Conference on Coastal Engineering, Am. Soc. of Civ. Eng., Copenhagen, 1998.

Zedel, L., and A. E. Hay, A Coherent Doppler Profiler for high resolution particle velocimetry in the ocean: Laboratory measurements of turbulence and particle flux, *J. Atmos. Oceanic Technol.*, *16*, 1102–1117, 1999.

Zedel, L., and A. E. Hay, A three component bistatic Coherent Doppler velocity Profiler: Error sensitivity and system accuracy, *IEEE J. Oceanic Eng.*, *27*, 717–725, 2002.

Zedel, L., A. E. Hay, R. Cabrera, and A. Lohrmann, Performance of a single beam, pulse-to-pulse Coherent Doppler Profiler, *J. Atmos. Oceanic Technol.*, *21*, 290–297, 1996.

A. E. Hay and C. Smyth, Department of Oceanography, Dalhousie University, Halifax, NS, B3H 4J1, Canada. (csmyth@phys.ocean.dal.ca; alex.hay@dal.ca)